

# Evolution of Structural and Electronic Properties in NbTe<sub>2</sub> under High Pressure

Shujia Li,\* Qing Dong, Jiajia Feng, Yanju Wang, Mingqiang Hou, Wen Deng, Resta A. Susilo, Nana Li, Hongliang Dong, Shun Wan, Chunxiao Gao,\* and Bin Chen\*

Cite This: *Inorg. Chem.* 2021, 60, 7857–7864

Read Online

HPSTR  
1183-2021

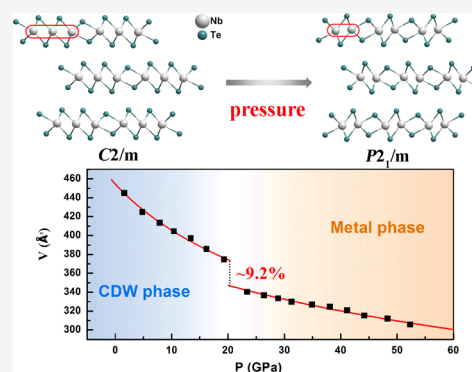
ACCESS |

Metrics & More

Article Recommendations

Supporting Information

**ABSTRACT:** Transition metal dichalcogenides (TMDs) have attracted wide attention due to their quasi-two-dimensional layered structure and exotic properties. Plenty of efforts have been done to modulate the interlayer stacking manner for novel states. However, as an equally important element in shaping the unique properties of TMDs, the effect of intralayer interaction is rarely revealed. Here, we report a particular case of pressure-tuned re-arrangement of intralayer atoms in distorted 1T-NbTe<sub>2</sub>, which was demonstrated to be a new type of structural phase transition in TMDs. The structural transition occurs in the pressure range of 16–20 GPa, resulting in a transformation of Nb atomic arrangement from the trimeric to dimeric structure, accompanied by a dramatic collapse of unit cell volume and lattice parameters. Simultaneously, a charge density wave (CDW) was also found to collapse during the phase transition. The strong increase in the critical fluctuations of CDW induces a significant decline in the electronic correlation and a change of charge carrier type from hole to electron in NbTe<sub>2</sub>. Our finding reveals a new mechanism of structure evolution and expands the field of pressure-induced phase transition.



## INTRODUCTION

Transition metal dichalcogenides (TMDs) MX<sub>2</sub> are a class of compounds composed of transition metal, mainly of group IVB, VB, VIB, and chalcogen (S, Se, Te), which have attracted renewed interest owing to their graphene-like low-dimensional crystal structure and promising potential applications.<sup>1–4</sup> Monolayer TMDs share a common X–M–X sandwich formula, which can adopt either octahedral (1T) or trigonal prismatic (1H) coordination. Compounds of different elements tend to form the thermodynamically-preferred coordination. With different stacking order and periodicity, the sandwich-structural unit can form numerous polymorphs, such as 1T, 2H, 3R, 4H, 6R, and derived distorted structures.<sup>5</sup> Thus, TMDs provide extra degrees of freedom in interpolytypic phase transitions compared with other simple 2D materials, for example, graphene and h-BN, which don't have polytypes or strongly correlated electrons. The electronic structure and physical properties of TMDs are highly dependent on their crystalline structures. For example, the 2H compounds are primarily semiconductors, while many 1T compounds are semimetals.<sup>6</sup> Non-trivial topological band structure is commonly observed in the T<sub>d</sub> structure TMDs, which is considered to be the origin of a series of salient quantum phenomena.<sup>7,8</sup>

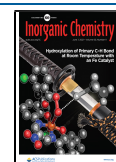
Pressure has been widely utilized in TMDs' investigation as a powerful tool to tune the Gibbs free energy of states, increase overlap of the local electron clouds thus promoting inter-

polytypic phase transitions and modulating electronic behavior away from pristine states. Recent studies show that structural modulation of TMDs by applying pressure is mainly reflected in the change of stacking style or interlayer spacing. For 2H and its derived polytypes, a representative example is the case of 2H-MoS<sub>2</sub>, in which pressure-induced isostructural phase transition from 2H<sub>c</sub> to 2H<sub>a</sub> through layer sliding was first reported.<sup>9</sup> Similar transformations have been found in other chalcogenides of molybdenum and tungsten.<sup>10–12</sup> For compounds with the parent structure of the 1T type, such as MoTe<sub>2</sub> and WTe<sub>2</sub>, pressure-induced transition from T<sub>d</sub> to 1T' structures are observed, owing to a lateral sliding of adjacent sandwich flats.<sup>6,13</sup> However, as an equally important factor in shaping the properties in TMDs, the intralayer interaction mechanism has never been revealed clearly. Here, we report the first example of pressure-tuned intralayer atoms re-arrangement in a distorted 1T-NbTe<sub>2</sub>, which demonstrates an entirely new type of structural phase transition in TMDs.

NbTe<sub>2</sub> is a kind of TMDs with peculiar distorted 1T structure, in which Nb atoms are polymerized into period-

Received: February 4, 2021

Published: May 20, 2021



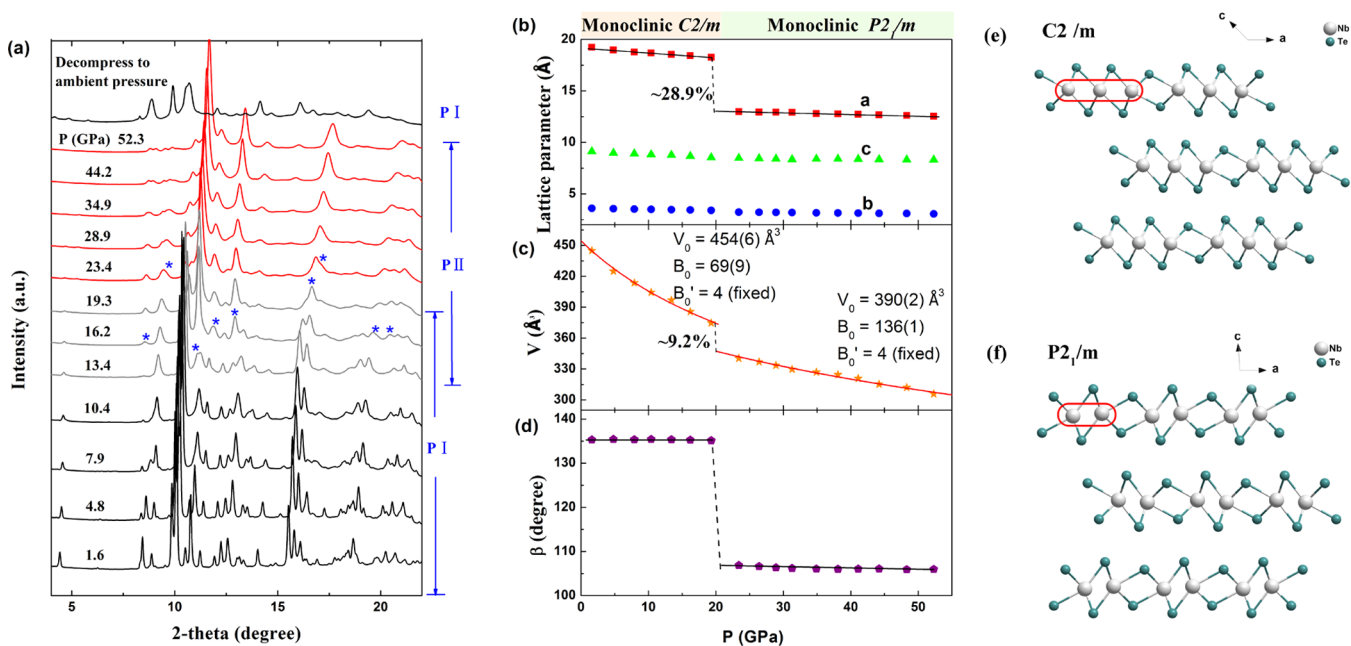


**Figure 1.** (a) Synchrotron XRD patterns for  $1T''$ - $\text{NbTe}_2$  at various pressures. The blue asterisks mark the appearance of new diffraction peaks. Pressure dependences of (b) lattice parameters  $a$ ,  $b$ ,  $c$ , (c) volume per formula unit, and (d) angle  $\beta$  of  $\text{NbTe}_2$ . Solid lines in (b,d) are guide to eyes. Solid lines in (c) are fitting results using Birch–Murnaghan equation. Structural diagrams of (f) the original  $1T''$  ( $C2/m$ ) phase and the (e) high pressure  $1T'$  ( $P2_1/m$ ) phase of  $\text{NbTe}_2$ .

tripling metal chains. This kind of polytype was reported as  $1T''$  or double-zig-zag structure, which is only observed in rare compounds including  $\text{NbTe}_2$  and  $\text{TaTe}_2$ .<sup>14</sup> The  $(3 \times 1 \times 3)$  superstructure observed in  $\text{NbTe}_2$  at room temperature suggests a robust commensurate charge density wave (CCDW) modulation.<sup>15,16</sup> It has been confirmed that the Fermi surface nesting and electron-phonon coupling both play a key role in the formation of CDW and in lowering of the crystal symmetry.<sup>17</sup> Recently,  $\text{NbTe}_2$  was predicted as a candidate of semimetal with topological protected band crossing,<sup>18</sup> which is considered to be related to a series of exotic electrical properties of  $\text{NbTe}_2$ , such as intrinsic superconductivity coexisting with CDW<sup>19–21</sup> and quantum linear magnetoresistance.<sup>22</sup> To date, the studies on electrical properties of compressed  $\text{NbTe}_2$  are limited to a pressure region lower than 20 GPa, and the information of structural evolution under pressure are absent. Zhang et al. reported the collapse of superconductivity when applied a pressure of 1.3 GPa on  $\text{NbTe}_2$ .<sup>21</sup> Vaidya et al. measured the electrical resistivity under pressure and found no abnormal change.<sup>23</sup> In addition, little is known about the properties of isostructural  $1T''$ - $\text{TaTe}_2$  under pressure. Thus, systematic studies on the structural and electronic phase diagram of  $\text{NbTe}_2$  under higher pressure are desperately important to extend the understanding of  $1T''$  polytypic TMDs.

In this work, the structural, vibrational, and electrical transport properties of compressed  $\text{NbTe}_2$  were systematically studied up to 58.9 GPa. A pressure-induced structural phase transition from  $1T''$  ( $C2/m$ ) to  $1T'$  ( $P2_1/m$ ) were found around 16–20 GPa through changing the intralayer arrangement of Nb atoms from trimeric to dimeric. The structural phase transition results in a collapse of unit cell volume and a dramatic change in lattice parameters. Simultaneously, the evolution of CDW order under pressure in  $\text{NbTe}_2$  is strongly coupled with the lattice structure. Raman scattering and electrical transport results suggest a possible CDW quantum

critical point (QCP) at the structural transition pressure. The strong increase in the critical fluctuations of CDW induces a significant decline of electron correlation and a change of dominant charge carrier type of compound from hole to electron in  $\text{NbTe}_2$ . Our finding provides a new perspective on the structural and electronic states evolution of TMDs under pressure.

## EXPERIMENTS

High-quality single crystals of  $1T''$ - $\text{NbTe}_2$  used in our measurements were grown by the chemical vapor transport method. The pressure was applied in a diamond anvil cell with 300  $\mu\text{m}$  culet. In situ high-pressure XRD experiments were performed at Beamline 12.2.2 in the Advanced Light Source, Lawrence Berkeley National Laboratory ( $\lambda = 0.4959 \text{ \AA}$ ). Raman spectra were collected on a micro-Raman spectrometer (HR Evolution) using a 473 nm  $\text{Ar}^+$  laser as the excitation source. The samples applied in XRD and Raman experiments were powder crystals, and silicon oil and argon was used as pressure-transmitting medium. Electrical and magnetic transport measurements were carried out using the standard four-point probe method, conducted in a Quantum Design's Physical Property Measurement System. All samples were cleaved to obtain fresh surfaces before the measurements. The single crystal was surrounded in the pressure-transmitting medium of silicon oil to ensure quasi-hydrostatic pressure conditions in a sample chamber. The samples remained in one piece throughout the experiments.

## RESULTS AND DISCUSSION

At ambient pressure,  $\text{NbTe}_2$  crystallizes in a monoclinic  $1T''$  structure with a space group of  $C2/m$  (no. 12). Niobium atoms are coordinated by tellurium atoms in a distorted octahedral environment. The buckled surface of the Te planes and the non-uniform Nb–Nb distances are observed (see Figure 1e). The X-ray diffraction (XRD) pattern of a powdered sample at ambient pressure and room temperature is shown in Figure S1. The in situ XRD patterns collected at room temperature and pressure up to 52.3 GPa is shown in Figure 1a. As the pressure

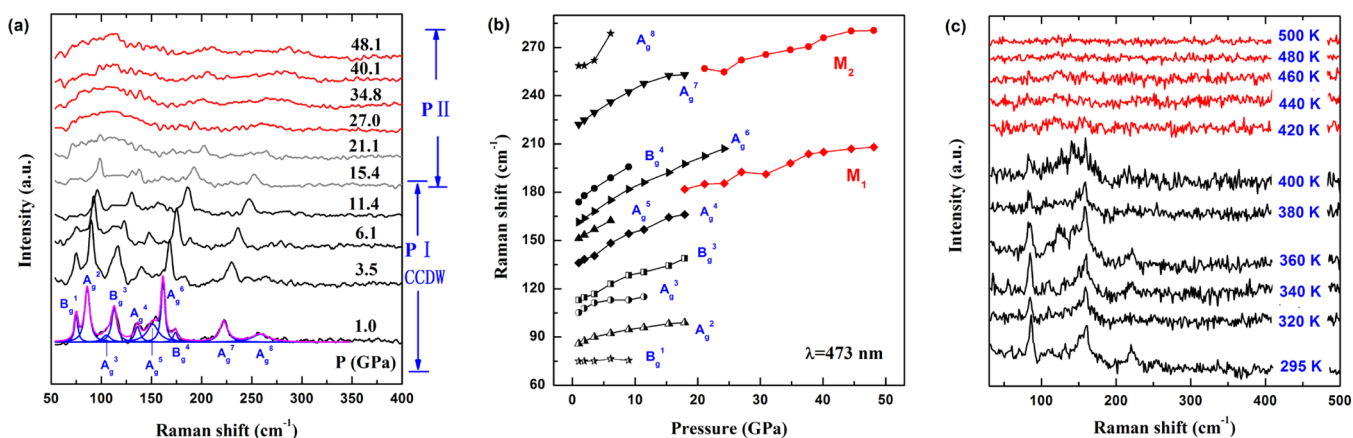


**Figure 2.** (a) Raman spectra of NbTe<sub>2</sub> at various pressures up to 48.1 GPa. The violet and blue lines are the peak fitting results of the Raman spectrum collected at 1.0 GPa. (b) Pressure dependence of phonon frequencies. (c) Raman spectra of NbTe<sub>2</sub> at room pressures and various temperatures.

**Table 1. Frequencies of the Raman Active Modes at Ambient Conditions<sup>a</sup>**

calculated, in ref 25 (monoclinic 1T'-NbTe <sub>2</sub> )	calculated, in ref 17 (trigonal 1T-NbTe <sub>2</sub> )	experimental, in this work	experimental, in ref 25
53.7			55.6
71.2		74.4	69.4
89.0		84.5	84.0
102.5			100.5
107.1		105.6	105.8
108.3	112.1	109.8	109.8
129.5		134.8	131.3
146.0		148.8	148.8
152.5	162.1	159.1	158.7
173.9		170.2	169.7
220.9		219.8	218.2
253.1		254.5	253.2

<sup>a</sup>A comparison between the results in this work and previous works.

increases, all diffraction peaks shift to higher angles. The original structure remains stable until 13.4 GPa, at where a new characteristic peak appears around 11.1°, indicating the onset of a phase transition. The intensity of this new peak rapidly increases and becomes the strongest peak of the high-pressure phase at higher pressure. As the pressure increases to 16.2 GPa, the two strongest peaks of the original phase, (-6, 0, 3) and (3, 1, 0), weaken. The peak around 11.8° splits into two peaks. Other four new characteristic peaks show up at 8.5, 12.9, 19.8, and 20.4° respectively. With further compression to 23.4 GPa, new characteristic peaks arise at 9.4 and 17.1°. At this pressure, the phase transition is completed as no further changes in the diffraction patterns were observed. In the pressure range of 13.4–19.3 GPa, the XRD profiles contain the peaks from both low- and high-pressure phases. While in the pressure range of 23.4–52.3 GPa, all observed diffraction peaks belong to the new phase. The peaks remain unchanged except for a progressive right shift. When decompressing to the ambient pressure, the XRD pattern only contains the peaks of the original phase, confirming that the pressure-induced structural transition in NbTe<sub>2</sub> is reversible. The high-pressure phase can be well-indexed considering a monoclinic 1T' structure with the P2<sub>1</sub>/m space group (no. 11). The observed and refined profiles at 1.6 and 52.3 GPa are shown in Figure S2 for the 1T' (C2/m) and 1T' (P2<sub>1</sub>/m) phases.

The derived lattice parameters as functions of pressure are presented in Figure 1b–d. At ambient pressure, the lattice

parameters of original C2/m phase are  $a = 19.22 \text{ \AA}$ ,  $b = 3.61 \text{ \AA}$ ,  $c = 9.20 \text{ \AA}$ , and  $\beta = 135.32^\circ$ . As the pressure increases, the parameter  $b$  and  $c$  decrease in a linear trend, and no anomalous change is observed around the phase transition pressure. On the other hand, parameter  $a$  significantly reduces by about 28.9% and an anomalous change of the  $\beta$  angle from 135.1 to 106.9° emerges at the phase transition pressure. As shown in the structural diagram of Figure 1e,f, the Nb atoms in the C2/m phase are modulated to the period-tripling metal chains, while the Nb atoms in P2<sub>1</sub>/m phase are modulated to the period-doubling zigzag chains. The collapse of parameter  $a$  can be attributed to the change of periodicity along  $a$  axis during the phase transition. The change in the  $\beta$  angle indicates the existence of shear-derived relative slipping between adjacent layers. The volume-pressure relationship in both phases are fitted by the third-order Birch–Murnaghan equation of states<sup>24</sup>

$$P = \frac{3}{2}B_0 \left[ \left( \frac{V_0}{V} \right)^{7/3} - \left( \frac{V_0}{V} \right)^{5/3} \right] \left\{ 1 + \left( \frac{3}{4}(B'_0 - 1) \left[ \left( \frac{V_0}{V} \right)^{2/3} - 1 \right] \right) \right\} \quad (1)$$

where  $V_0$ ,  $B_0$ , and  $B'_0$  represent the unit cell volume, bulk modulus, and its first derivative at 0 GPa, respectively. In this case,  $B'_0$  is fixed to 4. The Birch–Murnaghan fitting to the data

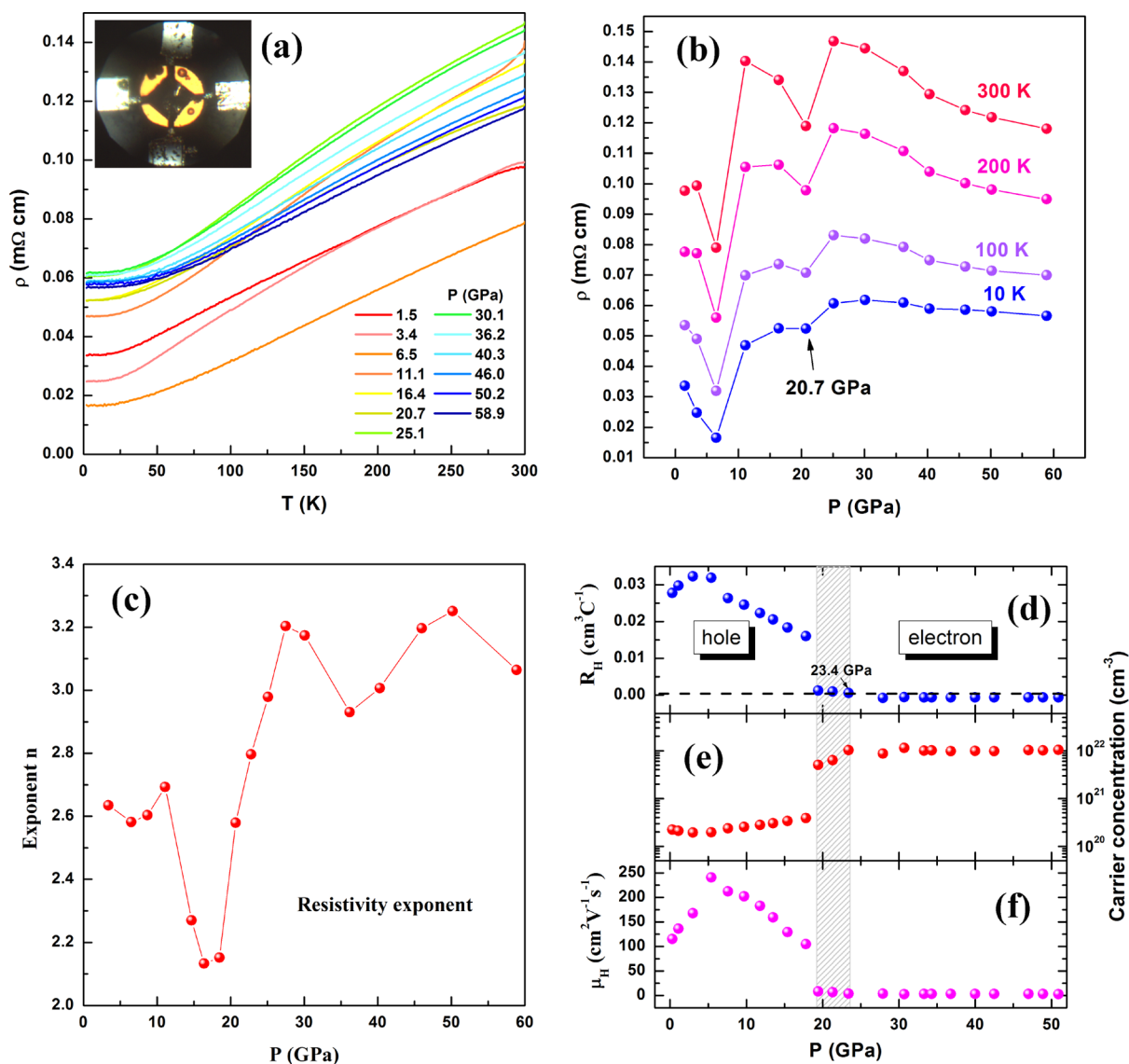


**Figure 3.** (a) Temperature-dependent resistivity of NbTe<sub>2</sub> at various pressures. The inset shows the photo of sample and electrode configuration in the experiment. (b) Pressure dependence of resistivity at 300, 200, 100, and 10 K. (c) The exponent  $n$  in the  $T$  dependence of  $\rho(T)$  at low  $T$ . The power-law fittings are adopted in the temperature range of 2–40 K. The pressure dependence of (d) Hall coefficient, (e) charge carrier concentration, and (f) Hall mobility. Data in (a–c) were gained in run 1. Data in (d–f) were gained in run 2. The data gained in run 3 are shown in Figure S7. In Hall effect measurements, the current is applied in the  $a$ – $b$  plane and the magnetic field is applied on the direction perpendicular to the  $a$ – $b$  plane.

yield  $V_0 = 454(6) \text{ \AA}^3$ ,  $B_0 = 69(9)$  for the low-pressure phase and  $V_0 = 390(2) \text{ \AA}^3$ ,  $B_0 = 136(1)$  for the high-pressure phase. The modulus of the high pressure phase is much larger than that of the low pressure phase, verifying that the sample become denser and more incompressible under pressure. The phase transition also leads to a contraction of the unit cell volume of about  $\sim 9.2\%$ .

The Raman vibrational modes are sensitive to the changes of structure and symmetry of materials. As shown in Figure 2a, the Raman spectra were collected at room temperature from ambient pressure to 48.1 GPa. The excitation laser wavelength is 473 nm. Compounds with the trigonal 1T structure share the common Raman-active vibrational modes, that is, an  $E_g$  mode representing the atomic vibrations within the  $a$ – $b$  plane and an  $A_g$  mode representing the atomic vibrations parallel to the  $c$  axis. Theoretical study by Battaglia et al. predicted the position of these two modes for undistorted trigonal 1T-

NbTe<sub>2</sub>, that is,  $E_g = 112.1 \text{ cm}^{-1}$  and  $A_g = 162.1 \text{ cm}^{-1}$ .<sup>17</sup> Actually, at room temperature, the structure of NbTe<sub>2</sub> modulated by the CCDW is much more complicated. The primitive cell of 1T'-NbTe<sub>2</sub> contains three Nb atoms and six Te atoms. Group theory analysis predicts 24 vibrational modes for NbTe<sub>2</sub> that is represented by

$$B_{\text{opt}} = 8A_g + 4A_u + 4B_g + 8B_u \quad (2)$$

Twelve modes ( $8A_g + 4B_g$ ) are Raman active, while the other twelve modes ( $4A_u + 8B_u$ ) are infrared-active. The  $A_g$  modes represent the atomic vibrations in the  $a$ – $c$  plane. The  $B_g$  modes represent the atomic vibrations parallel to the  $b$  axis. Barajas-Aguilar et al. calculated the position of these Raman peaks using density functional theory (DFT),<sup>25</sup> which conforms well to our measurement at the ambient pressure (see the comparison in Table 1).

When the external pressure is applied, all Raman peaks shift to the high wavenumber direction. Upon the compression to 9.0 GPa, the peaks of  $B_g^1$ ,  $B_g^4$ , and  $A_g^8$  modes disappear. With continuous compression to 15.4 GPa, the peak of  $A_g^3$  mode also vanishes. As the pressure increases up to 21.1 GPa, all vibration modes of the low-pressure phase are replaced by two new broad peaks around, 188.1 and 256.9  $\text{cm}^{-1}$  (named as  $M_1$  and  $M_2$  modes, respectively) and a broad feature between 80 and 120  $\text{cm}^{-1}$ . The Raman spectra gained in run 2, collected on a low-frequency Raman spectrometer, are shown in Figure S3. The  $M_1$  and  $M_2$  modes of high-pressure phase arise at  $\sim 125$  and 244  $\text{cm}^{-1}$  under a pressure of 17.5 GPa, which are consistent with the position of characteristic vibrational modes of  $\text{MoTe}_2$  and  $\text{WTe}_2$  crystalized in the 1T' structure.<sup>6,26,27</sup> It appears that the broad feature around 80–120  $\text{cm}^{-1}$  is not intrinsically of the sample, as it was not observed in run 2.

The re-arrangement of the intralayer metal atoms during the structural phase transition suggests a possible change in the CDW states. Raman vibration is an ideal probe for in situ detection of CDW transformation under pressure. We compared our Raman results with the Raman studies of isomorphic TMDs, 1T-TaS<sub>2</sub> and 1T-TiSe<sub>2</sub>. They have rich CDW phase diagrams. TaS<sub>2</sub> in the CCDW phase has a series of sharp and strong vibration peaks. When the translational symmetry is broken along the modulation direction, TaS<sub>2</sub> transforms to the in-CCDW (ICCDW) phase, Raman peaks become broader and weaker until they are difficult to distinguish from the background.<sup>28</sup> Similarly, broadened and disappearance of Raman peaks are also observed during the melting of the CDW state in 1T-TiSe<sub>2</sub>.<sup>29,30</sup> Previous studies showed that the CCDW order of NbTe<sub>2</sub> melted when beam heating was applied.<sup>15</sup> However, in situ characterization of the non-CDW metallic phase is lacking. We collected the Raman spectra at various temperatures, as shown in Figure 2c. In the high-temperature experiments, the sample was sealed in an argon atmosphere of  $\sim 0.5$  GPa to isolate the influence of oxygen in the air. When the temperature rises to 380 K, Raman peaks obviously becomes broadened and weakened with increasing temperature. When the temperature rises to above 420 K, all vibration modes disappear, indicating the melting CDW order in NbTe<sub>2</sub>. We propose that a similar mechanism occurred in the high-pressure experiments. In particular, Raman peaks begin to broaden when pressure rises to 11.4 GPa and vanish gradually as pressure rises to 21.1 GPa. The remarkable increase of full width at half-maximum (FWHM) (shown in Figure S4) and peak shape diverging from the Lorentz type observed in the high-pressure phase indicated the broken translational symmetry along the modulation direction.

The temperature-dependent resistivity measurements on the NbTe<sub>2</sub> single crystal from 2 to 300 K at various pressures are shown in Figure 3a. NbTe<sub>2</sub> presents a metallic conducting characteristic with  $\rho$  having a positive temperature coefficient at all experimental pressure conditions. The resistivity at 300 to 10 K shows consistent pressure dependence. As shown in the Figure 3b,  $\rho$  decreases rapidly from ambient pressure to 6.5 GPa and then presents an increasing trend. Around the pressure of 20.7 GPa,  $\rho$  deviates from the upward trend and shows an abnormal decline, corresponding to the structural phase transition. After 30 GPa, the resistivity decreases slowly with increasing pressure.

For further investigation, we analyzed the evolution of resistivity by using the power law,  $\rho(T) = \rho_0 + AT^n$ , where  $\rho_0$  is the residual resistivity related to impurity scattering,  $n$  is the

temperature exponent reflecting the dominant scattering mechanism of charge carrier, and the pre-factor  $A$  is related to the pairing interaction strength. The fitting is adopted over the temperature region of 2–40 K, and all  $\rho$ - $T$  curves are found to follow the power law (see Figure S5). The pressure dependence of temperature exponent  $n$  is shown in Figure 3c. The exponent  $n$  fluctuates around 2.6 in the low-pressure range and then shows a steep decline from  $\sim 2.6$  to  $\sim 2.1$  at 16.4 GPa. It begins to increase after 20 GPa. The exponent rises to the value of  $n \sim 3.0 \pm 0.2$  above 25 GPa. The abnormal decrease of  $n$  around the phase transition pressure provides another evidence of the CDW QCP. In previous studies, similar abnormal decrease of  $n$  were observed in TiSe<sub>2</sub> and Lu(Pt<sub>1-x</sub>Pd<sub>x</sub>)<sub>2</sub>In when accessing the CDW QCP.<sup>31,32</sup> Comparisons with the studies of well-understood antiferromagnetic QCP indicate that the exponent decrease can be regarded as a common feature of QCP, although precise value of exponent varies depending on the intrinsic properties of materials.<sup>33</sup> The decrease of exponent reflects a strong enhancement in the quantum fluctuations and a significant decline of electronic correlation when approaching the CDW QCP. In the high-pressure phase, exponent  $n$  varies around 3. The value  $n = 3$  was reported in rare cases including 1T-TiSe<sub>2</sub>,<sup>32</sup> Nb<sub>3</sub>Ge,<sup>34</sup> and Lu(Pt<sub>1-x</sub>Pd<sub>x</sub>)<sub>2</sub>In,<sup>31</sup> which can be attributed to a dominant phonon-assisted inter-band scattering. The abnormal decrease of  $\rho_{10\text{K}}$  around 20 GPa might also relate to the response of the system approaching CDW QCP.

Both Raman and electrical results confirm the collapse of CDW under pressure. However, the thermal hysteresis of CDW transition shown as a hump or a kink in the  $\rho$ - $T$  curve was not observed in NbTe<sub>2</sub>. The thermal hysteresis is always regarded as a characteristic of the CDW transition in some CDW materials.<sup>35</sup> Thus, it is difficult to determine the complete  $P$ - $T$  phase diagram of NbTe<sub>2</sub>. For reasons, first, the temperature gradient in DAC during the cooling and warming process would seriously hamper the measurement of thermal hysteresis. Second, in NbTe<sub>2</sub>, the atom displacement and Fermi surface reconstruction caused by CDW are moderate. Therefore, in NbTe<sub>2</sub>, the thermal hysteresis of CDW transition is relatively weak.

It has been established that the Hall coefficient ( $R_H$ ) is a very important parameter to characterize CDW transition. We measured the Hall resistivity and magnetoresistivity (MR) of NbTe<sub>2</sub> at 10 K under various pressures up to 50.9 GPa. The Hall coefficient, carrier concentration, and Hall mobility are shown in Figure 3d–f. From ambient pressure to 17.8 GPa, the  $R_H$  is positive. With continuous compression, the  $R_H$  decreases pronouncedly to almost zero and change the sign at a critical pressure of 23.4 GPa, indicating that the dominant carrier type changes from hole to electron. After that, the  $R_H$  is almost independent of pressure. The sign reversal of the Hall coefficient in NbTe<sub>2</sub> marks the collapse of CDW, as reported in the cases of NbSe<sub>2</sub>, TaS<sub>2</sub>, and TaSe<sub>2</sub>.<sup>36,37</sup> However, the  $R_H$  values measured in NbSe<sub>2</sub>, TaS<sub>2</sub> and TaSe<sub>2</sub> change from negative to positive before and after the collapse of CDW, presenting an inverse trend from NbTe<sub>2</sub>. The CDW phase of NbTe<sub>2</sub> possesses a high carrier concentration order of magnitude of  $\sim 10^{21} \text{ cm}^{-3}$ , indicating the existence of a relatively large Fermi surface. The collapse of CDW leads to a remarkable increase of carrier concentration of about thirteen times and induces an abrupt decrease of the Hall mobility, which indicates the close of the CDW gap that existed in certain regions of the Fermi surface.

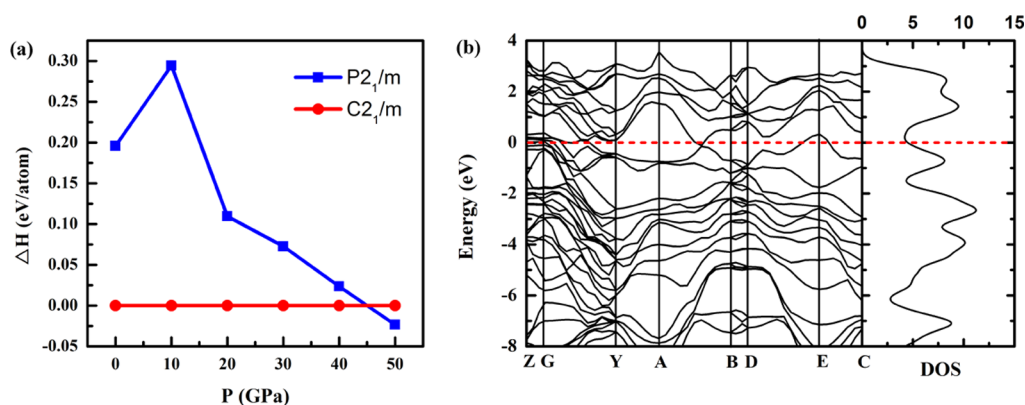


**Figure 4.** (a) Enthalpies (relative to the  $C2/m$  structure) as a function of pressure. (b) Band structure of the  $P2_1/m$  phase of  $NbTe_2$  at 50 GPa.

At 6.5 GPa, the resistivity changed from falling to rising trend. The Hall coefficient and Hall mobility also show turning points. All the special changes of the electrical parameter are indicative of a possible abnormality of the electronic structure. However, the XRD and Raman spectra did not show obviously abnormal changes around this pressure, indicating the stability of the crystal structure. More experiments are needed to clarify this anomaly.

The magnetoresistance under various pressures were measured by applying a field vertical to the  $a$ - $b$  plane up to 8 T (Shown in the Figure S6). The MR in the high-pressure phase is obviously suppressed compared to that in the low-pressure phase. At ambient pressure, an anomalous linear MR under high field is reported in  $NbTe_2$ .<sup>22</sup> The studies of the anisotropic linear MR behavior reveal that a large quasi-2D Fermi surface and small Fermi pockets with linearly dispersive bands coexist in  $NbTe_2$ . However, the quantum linear MR phenomenon is not observed in our high-pressure experiments.

We further calculated the enthalpies and band structure  $1T'$  ( $P2_1/m$ )  $NbTe_2$  using DFT, as shown in Figure 4. The predicted phase transition from enthalpies occurs around 45 GPa, which is higher than the phase transition pressure we observed in experiments. No negative frequencies for the acoustic phonons were observed, which confirms the dynamical stability of the  $P2_1/m$  structure under high pressure. The density of states (DOS) exhibits a pseudogap around the Fermi energy, indicating the semimetal character of  $P2_1/m$  structure. The increase of DOS at the Fermi energy of  $P2_1/m$  compared with that of the  $C2/m$  structure reflects the close of the CDW gap. In the theoretical calculation, ideal conditions of hydrostatic pressure and absolute zero were adopted, which are very different from the pressure and temperature conditions in experiments. The phase transition is driven by not only the relative enthalpy values of the two phases, but also many other factors, such as defects in material. This is probably the reason for the discrepancy between experiments and calculations.

Thus far, the results of XRD, electrical transport, and Raman spectrum together indicate a simultaneous structural and electronic phase transition. It provides us an insight into the mechanism of phase transition of  $NbTe_2$ . The stability of TMDs can be explained considering the relative strength of two competing mechanisms: ligand field stabilization of d-orbitals corresponding to the coordination geometry of transition metal and CDW instability with a periodic lattice distortion.<sup>38</sup> For many TMDs without CDW or with moderate CDW modulation, the  $2H$  polytype commonly has the highest

stability at ambient conditions. For  $NbTe_2$ , the strong modulation of CDW lowered the energy of parent  $1T$  polytype. Thus, trimeric-deformed version of the trigonal  $1T$  polytype becomes the only stable configuration of this compound in its natural state. As the application of pressure inhibits the modulation of CDW and modulates the Gibbs free energy of phases, the less-distorted dimeric  $1T'$  phase becomes more thermodynamically stable than the  $1T''$  phase above 20 GPa. A strong coupling exists between the change of the lattice structure and CDW order.

## CONCLUSIONS

In summary, structural phase transitions and electrical properties of  $NbTe_2$  under high pressure are reported. A structural phase transition from the  $1T''$  to  $1T'$  phase was found to occur between 16 GPa and 20 GPa, which results in a shrink of the unit cell volume by  $\sim 9.2\%$  and abrupt changes of the lattice parameter  $a$  and angle  $\beta$ . Through this phase transition, the intra-layer atomic structure is rearranged, that is, by changing the polymerization of Nb atoms from trimeric to dimeric. Raman scattering and electrical transport results confirmed a CDW QCP at the structural transition pressure and the CDW order melts to an incommensurate state. The sign reversal of the Hall coefficient from positive to negative as well as a significant decrease in MR above 20 GPa suggests that the phase transition from the  $1T''$  to  $1T'$  structure is accompanied by the change in the Fermi surface topology under pressure. The close of the CDW gap leads to an increase of the DOS at the Fermi level and carrier concentration. Our findings exhibit a unique example of modulating the intra-layer lattice structure of TMDs through applying external pressure. It provides a new perspective on the structural and electronic states changes of TMDs, which will motivate further experimental and theoretical studies on TMDs to explore the new structural transition mechanism.

## ASSOCIATED CONTENT

### Supporting Information

The Supporting Information is available free of charge at <https://pubs.acs.org/doi/10.1021/acs.inorgchem.1c00360>.

XRD pattern at ambient condition, refinement results, Raman spectra and FWHM at various pressures, power-law fitting of R-T curves, magnetoresistance at various pressures, and pressure-dependent resistivity at 300 K (PDF)

## ■ AUTHOR INFORMATION

## Corresponding Authors

**Shujia Li** – State Key Laboratory of Superhard Materials, Jilin University, Changchun 130012, China; Center for High Pressure Science and Technology Advanced Research, Shanghai 201203, China; [orcid.org/0000-0002-4933-9051](https://orcid.org/0000-0002-4933-9051); Email: [shujia.li@hpstar.ac.cn](mailto:shujia.li@hpstar.ac.cn)

**Chunxiao Gao** – State Key Laboratory of Superhard Materials, Jilin University, Changchun 130012, China; [orcid.org/0000-0001-5329-2623](https://orcid.org/0000-0001-5329-2623); Email: [cc060109@qq.com](mailto:cc060109@qq.com)

**Bin Chen** – Center for High Pressure Science and Technology Advanced Research, Shanghai 201203, China; Email: [chenbin@hpstar.ac.cn](mailto:chenbin@hpstar.ac.cn)

## Authors

**Qing Dong** – State Key Laboratory of Superhard Materials, Jilin University, Changchun 130012, China

**Jiajia Feng** – Center for High Pressure Science and Technology Advanced Research, Shanghai 201203, China

**Yanju Wang** – Center for High Pressure Science and Technology Advanced Research, Shanghai 201203, China

**Mingqiang Hou** – Center for High Pressure Science and Technology Advanced Research, Shanghai 201203, China; Institute of Meteoritics, Department of Earth and Planetary Sciences, University of New Mexico, Albuquerque, New Mexico 87131, United States

**Wen Deng** – Center for High Pressure Science and Technology Advanced Research, Shanghai 201203, China

**Resta A. Susilo** – Center for High Pressure Science and Technology Advanced Research, Shanghai 201203, China; [orcid.org/0000-0003-0799-7416](https://orcid.org/0000-0003-0799-7416)

**Nana Li** – Center for High Pressure Science and Technology Advanced Research, Shanghai 201203, China

**Hongliang Dong** – Center for High Pressure Science and Technology Advanced Research, Shanghai 201203, China

**Shun Wan** – Center for High Pressure Science and Technology Advanced Research, Shanghai 201203, China

Complete contact information is available at:

<https://pubs.acs.org/10.1021/acs.inorgchem.1c00360>

## Notes

The authors declare no competing financial interest.

## ■ ACKNOWLEDGMENTS

The authors acknowledge financial support from the National Natural Science Foundation of China (11674404) and the National Thousand Talents Program in China. We are grateful to the beamline station 12.2.2 of Advanced Light Source, Lawrence Berkeley National Laboratory, USA, for experimental support of high-pressure synchrotron XRD.

## ■ REFERENCES

(1) Zhang, Y. J.; Oka, T.; Suzuki, R.; Ye, J. T.; Iwasa, Y. Electrically switchable chiral light-emitting transistor. *Science* **2014**, *344*, 725–728.

(2) Qian, X.; Liu, J.; Fu, L.; Li, J. Quantum spin Hall effect in two-dimensional transition metal dichalcogenides. *Science* **2014**, *346*, 1344–1347.

(3) Wilson, J. A.; Yoffe, A. D. The transition metal dichalcogenides discussion and interpretation of the observed optical, electrical and structural properties. *Adv. Phys.* **1969**, *18*, 193–335.

(4) Xu, X.; Yao, W.; Xiao, D.; Heinz, T. F. Spin and pseudospins in layered transition metal dichalcogenides. *Nat. Phys.* **2014**, *10*, 343–350.

(5) Yang, H.; Kim, S. W.; Chhowalla, M.; Lee, Y. H. Structural and quantum-state phase transition in van der Waals layered materials. *Nat. Phys.* **2017**, *13*, 931–937.

(6) Qi, Y.; Naumov, P. G.; Ali, M. N.; Rajamathi, C. R.; Schnelle, W.; Barkalov, O.; Hanfland, M.; Wu, S. C.; Shekhar, C.; Sun, Y.; Suss, V.; Schmidt, M.; Schwarz, U.; Pippel, E.; Werner, P.; Hillebrand, R.; Forster, T.; Kampert, E.; Parkin, S.; Cava, R. J.; Felser, C.; Yan, B.; Medvedev, S. A. Superconductivity in Weyl semimetal candidate MoTe<sub>2</sub>. *Nat. Commun.* **2016**, *7*, 10038.

(7) Ali, M. N.; Xiong, J.; Flynn, S.; Tao, J.; Gibson, Q. D.; Schoop, L. M.; Liang, T.; Haldolaarachchige, N.; Hirschberger, M.; Ong, N. P.; Cava, R. J. Large, non-saturating magnetoresistance in WTe<sub>2</sub>. *Nature* **2014**, *514*, 205–208.

(8) Augustin, J.; Eyert, V.; Böker, T.; Frentrup, W.; Dwelk, H.; Janowitz, C.; Manzke, R. Electronic band structure of the layered compound T<sub>d</sub>-WTe<sub>2</sub>. *Phys. Rev. B: Condens. Matter Mater. Phys.* **2000**, *62*, 10812–10823.

(9) Chi, Z.-H.; Zhao, X.-M.; Zhang, H.; Goncharov, A. F.; Lobanov, S. S.; Kagayama, T.; Sakata, M.; Chen, X.-J. Pressure-Induced Metallization of Molybdenum Disulfide. *Phys. Rev. Lett.* **2014**, *113*, 036802.

(10) Kohulák, O.; Martoňák, R. New high-pressure phases of MoSe<sub>2</sub> and MoTe<sub>2</sub>. *Phys. Rev. B* **2017**, *95*, 054105.

(11) Duwal, S.; Yoo, C.-S. Shear-Induced Isostructural Phase Transition and Metallization of Layered Tungsten Disulfide under Nonhydrostatic Compression. *J. Phys. Chem. C* **2016**, *120*, 5101–5107.

(12) Wang, X. F.; Chen, X. L.; Zhou, Y. H.; Park, C. Y.; An, C.; Zhou, Y.; Zhang, R. R.; Gu, C. C.; Yang, W. G.; Yang, Z. R. Pressure-induced iso-structural phase transition and metallization in WSe<sub>2</sub>. *Sci. Rep.* **2017**, *7*, 46694.

(13) Xia, J.; Li, D.-F.; Zhou, J.-D.; Yu, P.; Lin, J.-H.; Kuo, J.-L.; Li, H.-B.; Liu, Z.; Yan, J.-X.; Shen, Z.-X. Pressure-Induced Phase Transition in Weyl Semimetallic WTe<sub>2</sub>. *Small* **2017**, *13*, 1701887.

(14) Chen, C.; Kim, H.-S.; Admasu, A. S.; Cheong, S.-W.; Haule, K.; Vanderbilt, D.; Wu, W. Trimer bonding states on the surface of the transition-metal dichalcogenide TaTe<sub>2</sub>. *Phys. Rev. B* **2018**, *98*, 195423.

(15) van Landuyt, J.; van Tendeloo, G.; Amelinckx, S. The direct imaging of two-dimensional charge density waves and of commensurate superlattices in NbTe<sub>2</sub> and TaTe<sub>2</sub>. *Phys. Status Solidi A* **1975**, *29*, K11–K13.

(16) Wilson, J. A. Questions concerning the form taken by the charge-density wave and the accompanying periodic-structural distortions in 2H-TaSe<sub>2</sub>, and closely related materials. *Phys. Rev. B: Condens. Matter Mater. Phys.* **1978**, *17*, 3880–3898.

(17) Battaglia, C.; Cercellier, H.; Clerc, F.; Despont, L.; Garnier, M. G.; Koitzsch, C.; Aebi, P.; Berger, H.; Forro, L.; Ambrosch-Draxl, C. Fermi-surface-induced lattice distortion in NbTe<sub>2</sub>. *Phys. Rev. B: Condens. Matter Mater. Phys.* **2005**, *72*, 195114.

(18) Tang, F.; Po, H. C.; Vishwanath, A.; Wan, X. Comprehensive search for topological materials using symmetry indicators. *Nature* **2019**, *566*, 486–489.

(19) Maaren, M. H. V.; Schaeffer, G. M. Some new superconducting group V dichalcogenides. *Phys. Lett. A* **1967**, *24*, 645–646.

(20) Nagata, S.; Abe, T.; Ebisu, S.; Ishihara, Y.; Tsutsumi, K. Superconductivity in the metallic layered compound NbTe<sub>2</sub>. *J. Phys. Chem. Solids* **1993**, *54*, 895–899.

(21) Zhang, X.; Luo, T.; Hu, X.; Guo, J.; Lin, G.; Li, Y.; Liu, Y.; Li, X.; Ge, J.; Xing, Y.; Zhu, Z.; Gao, P.; Sun, L.; Wang, J. Superconductivity and Fermi Surface Anisotropy in Transition Metal Dichalcogenide NbTe<sub>2</sub>. *Chin. Phys. Lett.* **2019**, *36*, 057402.

(22) Chen, H.; Li, Z.; Fan, X.; Guo, L.; Chen, X. Quantum linear magnetoresistance in NbTe<sub>2</sub>. *Solid State Commun.* **2018**, *275*, 16–20.

(23) Vaidya, R.; Bhatt, N.; Patel, S. G.; Jani, A. R.; Garg, A.; Vijayakumar, V.; Godwal, B. K. Electrical resistance measurements

under pressure on NbTe<sub>2</sub> single crystal. *High Pressure Res.* **2003**, *23*, 379–387.

(24) Birch, F. Finite elastic strain of cubic crystals. *Phys. Rev.* **1947**, *71*, 809.

(25) Barajas-Aguilar, A. H.; Irwin, J. C.; Garay-Tapia, A. M.; Schwarz, T.; Paraguay Delgado, F.; Brodersen, P. M.; Prinja, R.; Kherani, N.; Jimenez Sandoval, S. J. Crystalline structure, electronic and lattice-dynamics properties of NbTe<sub>2</sub>. *Sci. Rep.* **2018**, *8*, 16984.

(26) Ma, X.; Guo, P.; Yi, C.; Yu, Q.; Zhang, A.; Ji, J.; Tian, Y.; Jin, F.; Wang, Y.; Liu, K. Raman scattering in the transition-metal dichalcogenides of 1T'-MoTe<sub>2</sub>, T<sub>d</sub>-MoTe<sub>2</sub>, and T<sub>d</sub>-WTe<sub>2</sub>. *Phys. Rev. B* **2016**, *94*, 214105.

(27) Zhou, Y.; Chen, X.; Li, N.; Zhang, R.; Wang, X.; An, C.; Zhou, Y.; Pan, X.; Song, F.; Wang, B.; Yang, W.; Yang, Z.; Zhang, Y. Pressure-induced T<sub>d</sub> to 1T' structural phase transition in WTe<sub>2</sub>. *AIP Adv.* **2016**, *6*, 075008.

(28) Ramos, S. L. L. M.; Plumadore, R.; Boddison-Chouinard, J.; Hla, S. W.; Guest, J. R.; Gosztola, D. J.; Pimenta, M. A.; Luican-Mayer, A. Suppression of the commensurate charge density wave phase in ultrathin 1T-TaS<sub>2</sub> evidenced by Raman hyperspectral analysis. *Phys. Rev. B* **2019**, *100*, 165414.

(29) Snow, C. S.; Karpus, J. F.; Cooper, S. L.; Kidd, T. E.; Chiang, T. C. Quantum melting of the charge-density-wave state in 1T-TiSe<sub>2</sub>. *Phys. Rev. Lett.* **2003**, *91*, 136402.

(30) Holy, J. A.; Woo, K. C.; Klein, M. V.; Brown, F. C. Raman and infrared studies of superlattice formation in TiSe<sub>2</sub>. *Phys. Rev. B: Solid State* **1977**, *16*, 3628–3637.

(31) Gruner, T.; Jang, D.; Huesges, Z.; Cardoso-Gil, R.; Fecher, G. H.; Koza, M. M.; Stockert, O.; Mackenzie, A. P.; Brando, M.; Geibel, C. Charge density wave quantum critical point with strong enhancement of superconductivity. *Nat. Phys.* **2017**, *13*, 967–972.

(32) Kusmartseva, A. F.; Sipos, B.; Berger, H.; Forro, L.; Tutis, E. Pressure induced superconductivity in pristine 1T-TiSe<sub>2</sub>. *Phys. Rev. Lett.* **2009**, *103*, 236401.

(33) Löhneysen, H. v.; Rosch, A.; Vojta, M.; Wölfle, P. Fermi-liquid instabilities at magnetic quantum phase transitions. *Rev. Mod. Phys.* **2007**, *79*, 1015–1075.

(34) Woodard, D. W.; Cody, G. D. Anomalous Resistivity of Nb<sub>3</sub>Sn. *Phys. Rev.* **1964**, *136*, A166–A168.

(35) Feng, J.; Susilo, R. A.; Lin, B.; Deng, W.; Wang, Y.; Li, B.; Jiang, K.; Chen, Z.; Xing, X.; Shi, Z.; Wang, C.; Chen, B. Achieving Room-Temperature Charge Density Wave in Transition Metal Dichalcogenide 1T-VSe<sub>2</sub>. *Adv. Electron. Mater.* **2020**, *6*, 1901427.

(36) Zhao, X.-M.; Zhang, K.; Cao, Z.-Y.; Zhao, Z.-W.; Struzhkin, V. V.; Goncharov, A. F.; Wang, H.-K.; Gavriluk, A. G.; Mao, H.-K.; Chen, X.-J. Pressure tuning of the charge density wave and superconductivity in 2H-TaS<sub>2</sub>. *Phys. Rev. B* **2020**, *101*, 134506.

(37) Naito, M.; Tanaka, S. Electrical Transport Properties in 2H-NbS<sub>2</sub>, -NbSe<sub>2</sub>, -TaS<sub>2</sub> and -TaSe<sub>2</sub>. *J. Phys. Soc. Jpn.* **1982**, *51*, 219–227.

(38) K C, S.; Zhang, C.; Hong, S.; Wallace, R. M.; Cho, K. Phase stability of transition metal dichalcogenide by competing ligand field stabilization and charge density wave. *2D Mater.* **2015**, *2*, 035019.